Case studies of the impact of high-speed solar wind streams on the electron radiation belt at geosynchronous orbit: Flux, magnetic field, and phase space density

D. P. Hartley,[1] M. H. Denton,[1,2] J. C. Green,[3] T. G. Onsager,[3] J. V. Rodriguez,[3,4] and H. J. Singer[3]

Received 4 April 2013; revised 16 September 2013; accepted 18 October 2013; published 8 November 2013.

[1] Investigation of electron radiation belt dropouts has revealed the importance of a number of loss processes, yet there remains a lack of quantitative detail as to how these processes wax and wane between events. The overarching aim of this study is to address the issue of electron radiation belt dropouts. This is achieved using in situ observations at geostationary orbit from GOES-13 (pitch angle-resolved electron data and magnetic field measurements) to examine the outer electron radiation belt during three high-speed stream-driven storms. Analysis and interpretation are aided by calculation of the phase space density (PSD) as a function of the three adiabatic invariants. Our results confirm the importance of outward adiabatic transport as a mechanism for causing electron dropouts at geosynchronous orbit; however, study of the pitch angle distributions indicates that other loss mechanisms are also likely to be occurring during these high-speed solar wind stream (HSS)-driven storms. Two of the studied events exhibit similar evolutionary structure in their pitch angle distributions: (i) highly peaked distributions immediately prior to the dropout (ii) sharp transitions between peaked and isotropic and then subsequent butterfly distributions, and (iii) isotropic distributions at minimum flux shortly afterwards (dusk). We also address the difficulty in interpreting PSD calculations by comparing the T96 model magnetic field with that measured by GOES-13. Our results are intended as a first step in quantifying the timeline of events that occur in the radiation belts following the arrival of a HSS—particularly timely given the increase in HSS occurrence expected in the declining phase of the current solar cycle.

Citation: Hartley, D. P., M. H. Denton, J. C. Green, T. G. Onsager, J. V. Rodriguez, and H. J. Singer (2013), Case studies of the impact of high-speed solar wind streams on the electron radiation belt at geosynchronous orbit: Flux, magnetic field, and phase space density, *J. Geophys. Res. Space Physics*, *118*, 6964–6979 , doi:10.1002/2013JA018923.

1. Introduction

[2] The intensity of the outer radiation belt depends on complex physics connecting the global magnetosphere including the plasma sheet, the ring current, and the ionospheric plasma. All of these systems are modified when high-speed solar wind streams (HSSs) impact on the magnetosphere. Our goal is to unravel this coupling by analyzing several HSS events and their impact on the outer radiation belt.

[3] High-speed streams exhibit characteristic structure in the solar wind [e.g., *McPherron and Weygand*, 2006; *Tsurutani et al.*, 2006, and references therein]. Upon impact on the magnetosphere, HSSs are known to cause dramatic changes to the Earth's plasma populations [*Borovsky and Denton*, 2006], as well as driving electromagnetic waves which may lead to losses [e.g., *Elkington et al.*, 1999; *Mann et al.*, 2004; *Thorne*, 2010; *MacDonald et al.*, 2010]. HSSs cause morphological changes in the outer electron radiation belt [e.g., *Miyoshi et al.*, 2007; *Hudson et al.*, 2008; *Borovsky and Denton*, 2009; *Morley et al.*, 2010], the plasma sheet [e.g., *Denton and Borovsky*, 2009], the ring current [e.g., *Jordanova et al.*, 2012], the ionosphere-plasmasphere [e.g., *Denton et al.*, 2009; *Sojka et al.*, 2009], and the magnetotail [e.g., *Denton and Cayton*, 2011; *Borovsky and Denton*, 2011a].

[4] In the outer radiation belt, the arrival of a HSS is usually associated with a rapid decrease (*dropout*) in the measured electron flux [e.g., *Onsager et al.*, 2002; *Green et al.*, 2004]. The onset of this dropout usually occurs

[1]Physics Department, Lancaster University, Lancaster, UK.
[2]Space Science Institute, Boulder, Colorado, USA.
[3]National Oceanic and Atmospheric Administration, Boulder, Colorado, USA.
[4]Cooperative Institute for Research in Environmental Sciences, University of Colorado, Boulder, Colorado, USA.

Corresponding author: D. P. Hartley, Physics Department, Lancaster University, Lancaster, Lancashire LA14YB, UK. (d.hartley1@lancaster.ac.uk)

2169-9380/13/10.1002/2013JA018923

after the passage of the interplanetary magnetic field (IMF) sector reversal prior to the passage of the corotating interaction region stream interface [*Borovsky and Denton*, 2009]. Following the dropout is a subsequent increase (*recovery*) in electron flux some hours or days later [*Freeman*, 1964; *Nagai*, 1988; *Chen et al.*, 2007]. In many instances, the electron flux may recover to a level greater than that prior to HSS arrival [*Miyoshi and Kataoka*, 2008; *McPherron et al.*, 2009]. *Reeves et al.* [2003] found that about half of geomagnetic storms increased the fluxes, about one in five storms decreased the fluxes, and the remaining storms produced changes that were less than a factor of two either up or down. The precise cause of the dropout has been variously associated with a number of processes [e.g., *Friedel et al.*, 2002; *Shprits et al.*, 2008a, 2008b] including (i) transport, both adiabatic and nonadiabatic (the electrons move away from the detector, for example, via inward or outward radial diffusion), (ii) loss to the atmosphere (as wave-particle interactions cause electrons to temporarily populate the bounce-loss cone), and (iii) loss to the magnetopause (as wave-particle interactions cause electrons to temporarily populate the drift-loss cone). Evidence for these processes, along with various combinations, has been uncovered by numerous authors although there remains a lack of quantitative detail as to how these processes wax and wane between different events. *Borovsky and Denton* [2009] suggest electromagnetic ion cyclotron waves as the primary cause of HSS-driven relativistic-electron dropouts, whereas *Turner et al.* [2012] suggest outward radial transport with losses being primarily to the magnetopause. Additionally, *Meredith et al.* [2011] concluded that there is no evidence for enhanced precipitation of relativistic electrons during the MeV flux drop out, although noted that precipitation of lower energy electrons did become enhanced during the passage of the high-speed stream. Although aspects of the physics involved are known, a complete and accurate physical understanding, and predictive capability, remains elusive.

[5] In this study we first analyze the quiet day variation of the electron radiation belt in order to provide a baseline from which to compare the impact of different HSS-induced dropout events. We then present case studies of three HSS-induced dropouts, focusing on measured electron flux, calculated phase space density, and pitch angle distribution variations in order to investigate the loss mechanisms that drive these rapid electron reductions. Studying these parameters, in addition to the geomagnetic field, allows us to build up a picture of the different processes that drive the variation of the electron radiation belt.

2. Analysis Method and Instrumentation

[6] The Magnetospheric Electron Detector (MAGED) onboard GOES-13 [*GOES N Databook*, 2009] provides pitch angle-resolved flux measurements in the 30–600 keV energy range. Consisting of nine telescopes, each with a central pitch angle, α, defined by the orientation of the magnetic field at any time instant, MAGED measures flux in five energy channels parametrized as 30–50, 50–100, 100–200, 200–350, and 350–600 keV. The fluxes are dead time and proton-contamination corrected. Converting to differential flux gives central energies of 40, 75, 150, 275, and 475 keV. A magnetometer measures the three orthogonal components of the magnetic field within a range of $\pm$512 nT and is accurate to $\pm$ a few nT.

[7] In this study we perform a fit of the flux pitch angle distribution for each 1 min interval along the orbit following the method of *Selesnick and Blake* [2000] (for full details, see appendix). It is then possible to extrapolate electron flux values at all pitch angles. This allows us to calculate the pitch angle anisotropy between perpendicular (α = 90°) and parallel (α = 15°) orientation for each energy channel where pitch angle anisotropy is parametrized as the electron flux at 15° divided by the electron flux at 90° ($\parallel$ / $\perp$). Additionally, we calculate the omnidirectional electron flux measurement from all nine telescopes of GOES-13 at 1 min time intervals. This allows for a single flux measurement (hereby referred to as electron flux, unless a specific pitch angle/orientation is stated) to be presented at each energy at each instance of time.

[8] Trapped radiation belt electrons undergo three characteristic types of motion; gyromotion about magnetic field lines, bounce motion along magnetic field lines between the mirror points, and drift motion around the earth. Each type of motion has an associated adiabatic invariant. These invariants remain conserved so long as changes to the magnetic field occur on time scales longer than the associated particle motion period (adiabatic). Violation of these invariants results in magnetospheric changes that are irreversible (nonadiabatic). Following the techniques used by *Green and Kivelson* [2004], we use ONERA-DESP IRBEM library [*Boscher et al.*, 2008], T96 magnetic field model [*Tsyganenko and Stern*, 1996], and in situ magnetic field measurements to calculate the phase space density (PSD) as a function of the three adiabatic invariants, μ (calculated using magnetic field from GOES), K, and L^* (calculated using T96 magnetic field model). The values chosen were μ = 500 MeV/G (as this represents the 350–600 keV energy channel from GOES-13) and K = 2500 $G^{1/2}$km or $K\sim$ 0.4 $G^{1/2}R_E$ (as it equates to a pitch angle between $\sim$15° and $\sim$35°). Permitted input values to the T96 magnetic field model include $-100 \leq Dst(\mathrm{nT}) \leq 20, 0.5 \leq P_{\mathrm{SW}}(\mathrm{nPa}) \leq 10$, $|By_{\mathrm{IMF}}|(\mathrm{nT}) \leq 10$, $|Bz_{\mathrm{IMF}}|(\mathrm{nT}) \leq 10$. Where required input values exceed the maximum permitted, the maximum value is used (as is the case with P_{SW} at times during this study). *Huang et al.* [2008] showed that for storms where the *Dst* index does not go below –60 nT (as is the case in all examples presented here), the T96 magnetic field model predicts magnetic field components that lie within nonstorm magnetospheric fluctuations.

[9] Calculating the phase space density with fixed values of the first and second adiabatic invariants allows us to observe how the L^* parameter, in addition to the phase space density itself, varies over the periods of interest. Observing variations in L^* provides insight as to whether electrons are being adiabatically transported either inward or outward. It is noted that PSD calculations are subject to limitations in the accuracy of the implemented magnetic field model. It is also noted that the calculation of L^* returns a value regardless of double minima along dayside field lines, where radiation belt particles undergo drift orbit bifurcation and thus cannot be associated with a specified drift shell [e.g., *Ukhorskiy et al.*, 2011].

[10] The implications of errors in the magnetic field model can be understood. Figure 1 displays the effect of

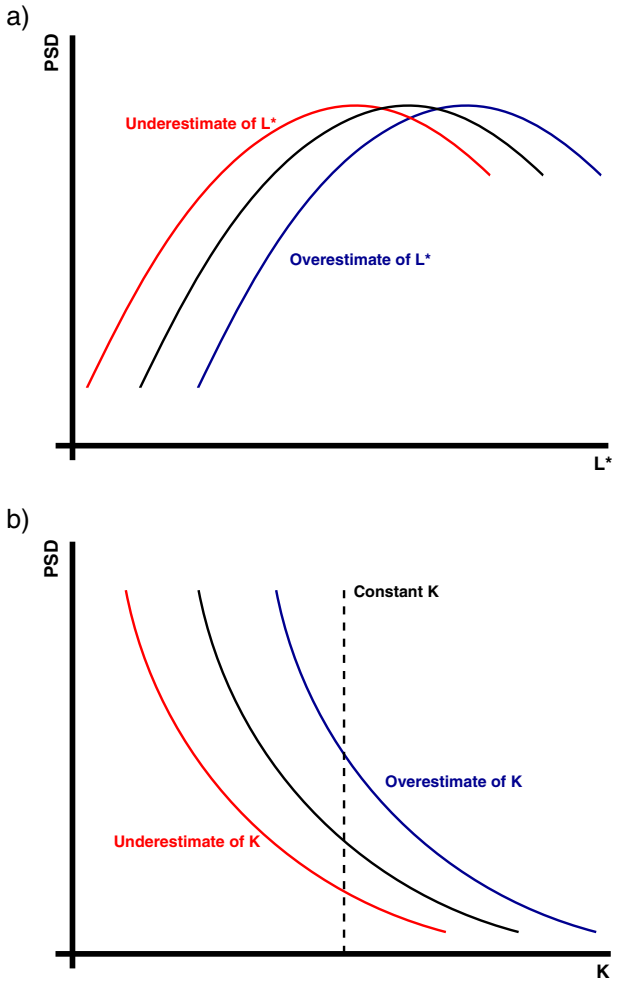

Figure 1. (a) Schematic representation of how an error in the calculation of the inverse of the third adiabatic invariant, L^*, will affect the predicted phase space density. (b) Schematic representation of how an error in the calculation of the second adiabatic invariant, K, will affect the predicted phase space density (after *Green and Kivelson* [2004]).

errors in calculating L^* and K on the PSD as in *Green and Kivelson* [2004]. If the model overestimates/underestimates the magnetic field magnitude, this leads to an overestimate/underestimate of L^* which, in turn, affects the calculated PSD as shown in Figure 1a. An underestimate of L^* leads to an underestimate of the PSD at high L^* and an overestimate of the PSD at low L^*. An overestimate of L^* leads to an overestimate of the PSD at high L^* and an underestimate of the PSD at low L^*. Since the second adiabatic invariant, K, depends upon the length of the magnetic field line as well as the magnetic field strength along it, any discrepancies between the model and actual magnetic field magnitude and stretching component will affect the calculation. Therefore, if the implemented model predicts an overstretched/understretched magnetic field, then this yields an underestimate/overestimate of the K and if the implemented model overpredicts/underpredicts the magnetic field magnitude, then this leads to an overestimate/underestimate of the K. This has implications on the calculated PSD as shown in Figure 1b; an overestimate of K yields an overestimate of the PSD at the chosen K, whereas an underestimate of K yields an underestimate of the PSD at the chosen K.

[11] First, a quiet day is studied in order to understand the behavior of the fluxes and PSD and to evaluate the performance of the T96 model during quiet geomagnetic conditions. Subsequently, three dropout events are examined with periods of interest shown in Table 1. Additionally, Table 1 lists specific details for each event; maximum and minimum solar wind velocities, maximum flow pressure, maximum and minimum fluxes, maximum and minimum *Dst* index, and maximum *Kp* index. The selection of these HSS-driven events was performed through observations of solar wind parameters, identifying the characteristic HSS structure (increase in solar wind velocity, density pulse straddling the boundary between slow and fast solar wind, shear flow).

3. Quiet Time Variation

[12] In order to observe the behavior of electron flux and calculated phase space density at geosynchronous orbit (GEO) during quiet time, a single day (30 January 2011) was examined, where the solar and geomagnetic conditions were calm and stable. Figure 2 displays a variety of parameters for this quiet period. Figure 2a shows the solar wind velocity (V_{SW}) and solar wind flow pressure from OMNI 2 [*King and Papitashvili*, 2005]. Figure 2b displays geomagnetic indices *Kp*, *Dst*, and SYM-H in addition to *Dst** (the pressure corrected *Dst* index), calculated using the methodology of *Borovsky and Denton* [2010]. Figure 2c shows the magnetic field magnitude as measured by GOES-13 at GEO and the predicted magnetic field magnitude from the T96 model at the location of GOES-13. In addition, an indicator of the "goodness" of the model fit to the observed magnetic field is displayed in color at the top of the panel: green indicates that the model is within ±15% of the measured magnetic field, yellow indicates ±30%, orange ±45%, and red ± > 45%.

$$\theta_{\text{stretch}} = \arctan(B_Z/(B_X^2 + B_Y^2)^{1/2}) \quad (1)$$

Table 1. Solar Wind and Geophysical Parameters for the Events in This Study; Maximum/Minimum Solar Wind Velocity, Maximum Solar Wind Pressure, Maximum/Minimum Flux Observed by GOES-13 in the 475 keV Electron Channel, Maximum/Minimum Dst Index, and Maximum *Kp* Index

Event	Start Time	End Time	V_{max} (km/s)	V_{min} (km/s)	P_{max} (nPa)	log_{10} ($flux_{max}$)	log_{10} ($flux_{min}$)	Dst_{max} (nT)	Dst_{min} (nT)	Kp_{max}
Quiet	30 Jan 2011 0 UT	31 Jan 2011 0 UT	299.5	270.3	1.80	1.697	1.222	7	–4	3.0
Event 1	6 Jan 2011 16 UT	7 Jan 2011 16 UT	551.0	327.8	15.2	2.268	–0.361	24	–38	5.0
Event 2	4 Feb 2011 12 UT	5 Feb 2011 12 UT	678.2	360.6	15.2	2.820	–0.277	21	–59	5.7
Event 3	11 Apr 2011 12 UT	12 Apr 2011 12 UT	630.7	312.0	17.4	2.945	–0.995	32	–51	5.0

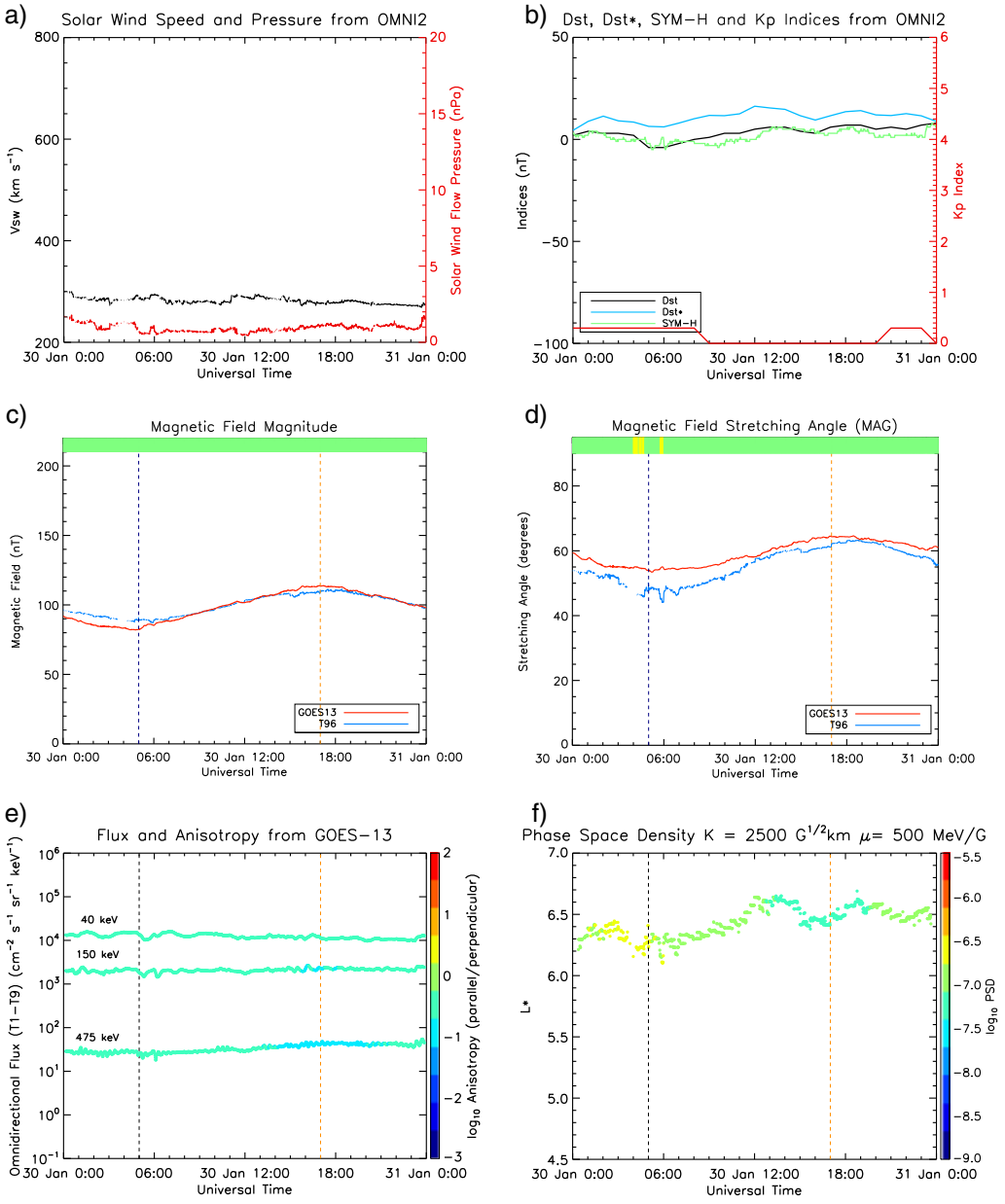

Figure 2. Quiet time variation: 0 UT 30 January to 0 UT 31 January. (a) Solar wind speed (black) and solar wind flow pressure (red) from OMNI2. Horizontal dashed red line indicates the maximum flow pressure that can be used in the T96 magnetic field model, 10 nT. (b) Geomagnetic indices *Dst*, *Dst** (calculated using methodology of *Borovsky and Denton* [2010]), SYM-H, and *Kp* indices. (c) The magnetic field magnitude output from the T96 magnetic field model in addition to the magnetic field as measured in situ by GOES-13. (d) The magnetic field stretching angle as output by T96 in addition to the stretching angle measured by GOES-13. Stretching angle is in centered dipole coordinates. In addition, an indicator of the "goodness" of the model fit to the observed magnetic field is displayed in color at the top of the panel: green indicates that the model is within ±15% of the measured magnetic field, yellow indicates ±30%, orange ±45%, and red ± > 45%. (e) Omnidirectional flux measurements for three energy channels from GOES-13 where color coding is electron anisotropy (warm colors indicating parallel orientation and cold colors indicating perpendicular orientation). (f) The phase space density as a function of time and L^* with fixed values of μ and K (μ = 500 MeV/G and K = 2500 G$^{1/2}$km or $K \sim 0.4$ G$^{1/2}R_E$). In Figures 2c to 2f, vertical dashed orange and black lines indicate local noon and midnight, respectively.

[13] Figure 2d displays the magnetic field stretching angle in centered dipole coordinates (MAG) as defined in equation (1) of both the measured field from GOES-13 and the predicted magnetic field from the T96 model at the GOES-13 position. This panel also displays an indication of goodness of fit of the model-stretching angle to the observations with the colors parameterized the same as in Figure 2c. Figure 2e shows the omnidirectional electron flux measurements averaged over all nine look directions for three energy channels from GOES-13 in addition to their pitch angle anisotropy in relation to the measured magnetic field. Figure 2f shows the calculated phase space density as a function of time and L^* with fixed values of μ and K (μ = 500 MeV/G and K = 2500 $G^{1/2}$km ($\sim$ 0.4 $G^{1/2}R_E$)).

[14] The solar wind speed remains relatively constant around 300 km s^{-1} for the entire period with the solar wind flow pressure remaining less than 2 nPa. The *Kp* index remains very low for the duration of the quiet period with geomagnetic indices *Dst*, *Dst**, and SYM-H showing no large disturbances. The magnetic field magnitude is slightly greater on the dayside than the nightside due to the compression by the solar wind. The magnetic field stretching angle, defined in equation (1), describes the shape of the magnetic field lines as measured at GOES-13.

[15] An angle closer to 90° indicates a largely dipolar field (since GOES-13 is at approximately 11° geomagnetic latitude, the stretching angle will normally be less than 90° unless the magnetosphere is compressed) whereas a smaller angle indicates a highly stretched field. Hence, the compression on the dayside gives a more dipolar field (stretching angle close to 90°) with a more stretched field on the nightside (smaller stretching angle) as is expected during quiet conditions. In this study we display the magnetic field stretching angle in centered dipole coordinates (MAG) in order to remove any seasonal effects. The T96 magnetic field model yields results that accurately follow the measurements from GOES-13 (within ±15% in magnitude and stretching angle for the vast majority of the period). Electron flux measurements from GOES-13 remain steady during this quiet period displaying very little variation in magnitude. The pitch angle anisotropy is as expected considering drift shell splitting; the electron pitch angle distribution is more perpendicularly oriented on the dayside than the nightside and vice versa with relatively smooth transitions between the two. This can also be seen in the complete pitch angle distribution (see Figure 6a). Such variations are not caused by changes in the omnidirectional electron flux, rather variations in the pitch angle distribution around the spacecraft orbit, and must be considered when interpreting data for active periods. The L^* parameter from the PSD calculation during this time varies between around 6.1 and 6.7. The phase space density for this period remains relatively steady with only minor variations. These variations may be due to PSD gradients in L^* (since the drift shell contours are not circles at geosynchronous orbit, we sample a range of L^*) or errors introduced by the magnetic field model. This "noise" in the PSD calculation must also be considered when analyzing active periods (small-scale changes in PSD may not necessarily be attributable to a physical process. For larger variations, it is more likely that the noise is being dominated by the process driving the variations).

4. Event 1: 6 January 2011

[16] Figure 3 contains plots of the same parameters as described for Figure 2 for the period of interest highlighted for Event 1 in Table 1.

4.1. Solar Wind and Geomagnetic Conditions

[17] The solar wind structure (see Figure 3a) is characteristic of a HSS with an initial calm period [*Borovsky and Steinberg*, 2006] with slow solar wind speeds. The solar wind speed then exhibits a clear increase, remaining elevated for several days. A density pulse arises due to the interaction between slow and fast solar wind, thus producing a peak in the flow pressure. The corotating interaction region consists of compressed slow solar wind followed by compressed fast solar wind. At around ∼15 UT 6 January, the *Kp* index increases abruptly, indicating the onset of enhanced convection, and remains elevated for around 2 days (see Figure 3b. In addition, the geomagnetic disturbance due to the HSS arrival is evident in *Dst*, *Dst**, and SYM-H indices.

4.2. Flux

[18] Electron flux and pitch angle anisotropy are shown in Figure 3e, with the full pitch angle distribution shown in Figure 6b. Between 16 and 21 UT 6 January, prior to the dropout, the flux of 475 keV electrons increases steadily while the pitch angle distribution becomes progressively more perpendicular oriented. Immediately prior to the dropout (around dusk local time), the electron distribution is extremely perpendicularly oriented. From 21 to 23 UT, a large reduction in the electron flux is observed (almost 2 orders of magnitude), with the pitch angle distribution becoming highly parallel oriented toward 23 UT. From this point, the flux continues to reduce by a further order of magnitude, reaching a minimum around 1 UT 7 January. During this reduction, the pitch angle distribution becomes approximately isotropic. From 1 to 2 UT 7 January, we observe a recovery in the electron flux by approximately 1 order of magnitude. From 2 UT until the end of the period of interest at 10 UT, the electron flux recovers steadily.

4.3. Pitch Angle Distribution

[19] The pitch angle distribution (see Figure 6b) is peaked (higher fluxes close to 90°, GOES-13 on the dayside) prior to the dropout, becoming increasingly peaked as the dropout approaches (21 UT 6 January, increasing pressure). This can be seen by increasing fluxes close to 90° and decreasing fluxes around 0° and 180°. As the dropout occurs (21 UT 6 January), the pitch angle distribution becomes more isotropic with increasing fluxes around 0° and 180° and decreasing fluxes around 90°. At around 22:30 UT 6 January, the flux around 90° suddenly reduces by several orders of magnitude while the flux closer to 0° and 180° also decreases but at a much slower rate. By around 1 UT 7 January, the electron flux has dropped out across the entire pitch angle distribution. Following this time, the flux begins to recover, first at more parallel pitch angles (butterfly distribution, GOES-13 on the nightside) with perpendicular electrons returning later. The pitch angle distribution displays the following sequence during this dropout event: (i) peaked distribution, (ii) increasingly peaked distribution immediately prior to dropout, (iii) reduction around 90° and increase

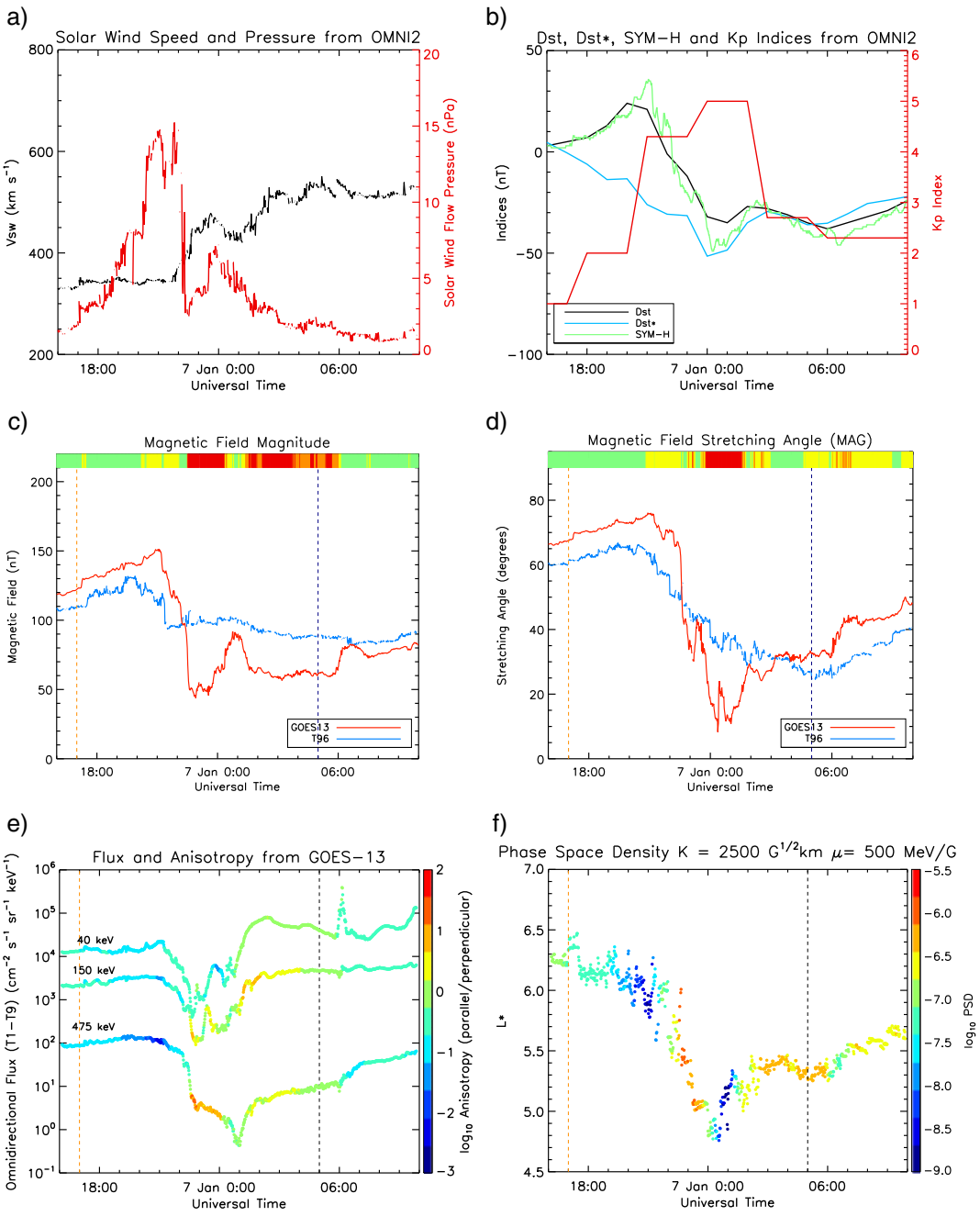

Figure 3. Event 1: 16 UT 6 January to 10 UT 7 January. The figure displays the same parameters as described in Figure 2.

around 0° and 180° leading to more isotropic distribution, (iv) sudden loss around 90° leading to butterfly distribution, (v) decay of butterfly distribution to become isotropic (minimum flux), (vi) recovery as butterfly distribution, and (vii) recovery across all pitch angles.

4.4. Magnetic Field

[20] Magnetic field magnitude and stretching angle as measured by GOES-13 are displayed in Figures 3c and 3d. The magnetic field strength increases steadily between 16 and 21 UT from 120 nT to around 150 nT. The peak magnetic field strength measured by GOES-13 does not occur when the spacecraft is located at noon local time; rather, this peak is coincident with the onset of the dropout in the measured electron flux. From 21 to 23 UT, the magnetic field magnitude reduces from 150 nT to around 50 nT before increasing again between 23 UT 6 January and 1 UT 7 January from 50 nT to around 90 nT. The field then decreases to between 60 and 70 nT and remains at this magnitude for approximately 4 h (2–6 UT). Around 6 UT, the magnetic field magnitude increases by around 20 nT before remaining approximately constant until the end of the period of interest at 10 UT.

[21] The magnetic field stretching angle between 18 and 21 UT 6 January displays a steady increase from around 65 to 75°, indicating an increasingly dipolar field. The time

of largest stretching angle (most dipolar) is coincident with the onset of the dropout in the electron flux. The stretching angle then decreases slowly at first between 21 and 22 UT before rapidly decreasing from approximately 70° to 30° in the next hour (22–23 UT). At 23 UT, the magnetic field stretching angle increases by approximately 10° to around 40° before decreasing further to a minimum of around 10° (very highly stretched) just after 0 UT 7 January. Following this, we observe a brief spike in the stretching angle approximately 20° in magnitude between 0 and 1 UT 7 January before observing a steady increase in the stretching angle between 1 UT and the end of the period of interest at 10 UT.

4.5. Phase Space Density

[22] Calculated phase space density as a function of time and L^* with fixed values of μ and K (μ = 500 MeV/G and K = 2500 $G^{1/2}$km ($\sim$ 0.4 $G^{1/2}R_E$)) is shown in Figure 3f. Between 16 and 21 UT 6 January, the calculated phase space density reduces by approximately 1 order of magnitude with L^* slowly decreasing to around 5.8. Between 21 and 23 UT, the decrease in L^* hastens with the phase space density values increasing by around 2 orders of magnitude. Between 23 UT 6 January and 0 UT 7 January, we observe a plateau in L^* between 5.0 and 5.1 with the phase space density beginning to decrease. Around 0 UT 7 January, L^* decreases once more to between 4.7 and 4.9 with phase space density continuing to decrease. L^* then returns to between 5.0 and 5.1 around 1 UT with very low phase space density values. For the remainder of the period of interest, we observe L^* trend upward barring a small reduction as the spacecraft passes around midnight local time. The calculated phase space density remains highly dynamic during this period although is generally elevated as the electron flux increases during recovery.

4.6. Discussion

[23] Measurements from GOES-13 show two reductions in the electron flux that contribute to the dropout. First, a reduction from 21 UT to approximately 22:30 UT 6 January, then a secondary reduction occurring between 22:30 UT 6 January and 1 UT 7 January. During the first reduction in electron flux, the pitch angle anisotropy becomes steadily less perpendicular oriented before abruptly becoming highly parallel oriented at around 22:30 UT 6 January. This can be seen in the full pitch angle distribution in Figure 6b as a sudden loss of electrons around 90° (magnetopause losses). The lower energy electrons begin to return to GEO at this time (22:30 UT); however, the 475 keV electron flux continues to decrease, albeit less abruptly. During this second reduction, the pitch angle anisotropy shifts from parallel orientation to rather more isotropic. This shift occurs much slower than the initial change to parallel orientation. While the variation in L^* during the dropout indicates that radial transport, coupled with a radial gradient in the electron flux, could play a crucial role in reducing electron fluxes at GEO, it is noted that PSD calculations are very sensitive to the magnetic field and therefore any variation between the model output and the measured magnetic field could lead to errors in both PSD and L^*, thus affecting our interpretation (as described in Figure 1). These errors in magnitude are largest between 23:30 and 0:30 UT and 1:30 and 6:30 and largest in stretching angle between 23:30 and 1:30 UT, indicating that the PSD results may not be accurate during these times. The first reduction in electron flux (between 21 UT and 22:30 UT) occurs when the solar wind flow pressure is reducing, causing the geomagnetic field magnitude measured by GOES-13 to decrease. It therefore follows that outward adiabatic transport of electrons would occur shown by a reduction in L^*. Losses to the magnetopause may occur and are consistent with the shift in pitch angle anisotropy. Such losses may greatly affect the higher energy electron population due to their drift speed being higher than that of lower energy electrons. Therefore, for a given time period on an open drift shell, more high energy electrons are likely to escape the system than those with lower energy. The secondary reduction in 475 keV electron flux (between 22:30 UT 6 January and 1 UT 7 January) occurs during a period when the solar wind flow pressure is increasing, causing the geomagnetic field to increase in magnitude and become increasingly stretched. If we consider the period from 23 UT 6 January to 1 UT 7 January and only PSD values with an L^* between 5.0 and 5.1, it is apparent that the PSD decreases rapidly (2 orders of magnitude in around 2 h). This indicates that there is some other process, besides adiabatic transport, causing a reduction in electron flux at GEO. This could be outward radial diffusion caused by a steep radial gradient in the PSD following losses to the magnetopause as concluded by *Turner et al.* [2012], who attributed the dropout primarily to outward radial transport with losses being primarily to the magnetopause. In addition, given the fact that the pitch angle distribution is highly parallel oriented at this time, any pitch angle scattering from wave-particle interactions could efficiently cause concurrent losses to the atmosphere. While some authors have concluded that atmospheric losses are not significant during HSS-driven dropout events [*Morley et al.*, 2010; *Meredith et al.*, 2011; *Hendry et al.*, 2012], some also suggest precipitation immediately prior to the recovery [*Hendry et al.*, 2012; *Clilverd et al.*, 2013], indicating that precipitation into the atmosphere may not be the primary driver of flux dropouts but may certainly play a role and even be involved in a process that triggers the recovery. RBSP/BARREL [*Millan et al.*, 2013] conjunctions may be able to clarify the importance of atmospheric loss as a mechanism for contributing to radiation belt dropouts. Another possible contributing factor to the electron reduction between 22:30 UT 6 January and 1 UT 7 January is the inherent local time variation; electrons respond adiabatically to the extreme stretching of the magnetic field (dusk sector), resulting in flux asymmetry in local time [*Green et al.*, 2004]. It is noted however that the T96 output magnitude and the magnetic field measured in situ by GOES-13 display a large discrepancy (around 50 nT) during the time of this second reduction in electron flux which could indicate potential inaccuracies in PSD and L^* (as highlighted in Figure 1, overestimate of L^* causing an overestimate of PSD at high L^* and underestimate of PSD at low L^*).

[24] It appears that outward transport, adiabatic or otherwise, plays a key role in causing losses for this event, as concluded by *Turner et al.* [2012]. In addition, there appears to be some other mechanism, differing from adiabatic transport, causing losses to the system. This indicates a two-stage process of loss mechanisms causing the flux dropout at GEO for this event.

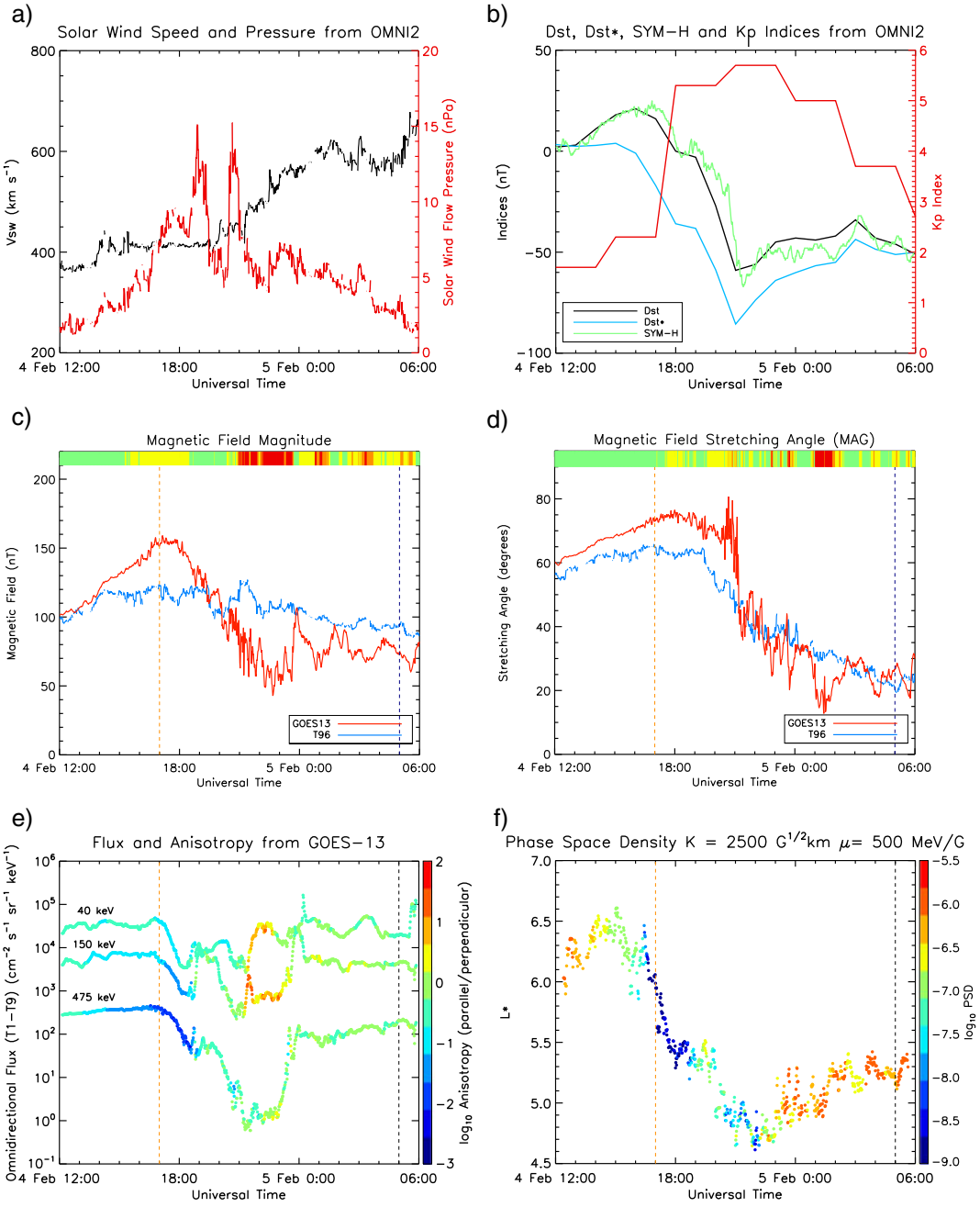

Figure 4. Event 2: 12 UT 4 February to 6 UT 5 February. This figure displays the same parameters as described in Figure 2.

5. Event 2: 4 February 2011

[25] Figure 4 displays the same parameters as described in Figure 2 for the period of interest highlighted for Event 2 in Table 1.

5.1. Solar Wind and Geomagnetic Conditions

[26] The solar wind speed displays a steady increase starting around 20 UT 4 February (see Figure 4a). The flow pressure becomes elevated around this increase as is characteristic of high-speed solar wind streams. The *Kp* index starts off relatively low before increasing sharply to above 5 at around 17 UT 4 February, indicating the onset of enhanced convection and the arrival of the HSS (see Figure 4b). The geomagnetic disturbance is evident in the *Dst*, *Dst**, and SYM-H indices starting at around 13 UT 4 February. *Dst* and SYM-H begin to become increasingly positive between 13 and 16 UT 4 February peaking around +20 nT before decreasing between 16 and 21 UT 4 February to a minimum between –60 and –70 nT.

5.2. Electron Flux

[27] Electron flux and pitch angle anisotropy are shown in Figure 4e, with the full pitch angle distribution shown in Figure 6c. From 12 UT to 17 UT on 4 February 2011, a slow steady increase in the flux of 475 keV electrons is observed. From 17 UT through 21 UT, the flux reduces by

more than 2 orders of magnitude. From being highly perpendicularly oriented prior to this dropout, the pitch angle anisotropy changes during the course of the event so that by the time of minimum flux, the pitch angle distribution appears to be largely isotropic. From this time, the electron population remains extremely low for approximately 2 h (∼21–23 UT) before abruptly increasing by around 2 orders of magnitude in a period of approximately 1 h (∼23–0 UT). The measured electron flux remains approximately constant and largely isotropic for at least 6 h following this period (0–6 UT).

5.3. Pitch Angle Distribution

[28] The pitch angle distribution (see Figure 6c) is initially isotropic with high fluxes across the entire pitch angle distribution. From 12 to 17 UT 4 February, the distribution becomes increasingly peaked with elevating flues close to 90° and decreasing fluxes around 0° and 180°. Between 17 and 19 UT, the fluxes reduce around 90° with a sharp boundary where the distribution becomes suddenly isotropic, possibly even butterfly, around 19 UT. The fluxes across the entire distribution then fall, with the minimum occurring between 21 and 23 UT. Following this, the flux begins to recover as a butterfly distribution (GOES-13 on the nightside). The pitch angle distribution follows the following sequence during this dropout event: (i) isotropic distribution, (ii) highly peaked distribution prior to dropout, (iii) reduction around 90° and increase around 0° and 180° leading to more isotropic, possibly even butterfly distribution, (iv) decay of butterfly distribution to become isotropic (minimum flux), and (v) recovery as butterfly distribution (GOES-13 on nightside).

5.4. Magnetic Field

[29] Magnetic field magnitude and stretching angle as measured by GOES-13 are displayed in Figures 4c and 4d. The magnetic field magnitude from 12 UT to 17 UT measured by GOES-13 displays a steady increase from 100 nT to 150 nT with the peak approximately coincident with when the spacecraft is located at noon local time. This is also the time that electron population begins to decrease. The magnetic field magnitude from 17 to 18 UT is steady at around 150 nT. Following this time, the magnetic field magnitude decreases from 150 nT to 50 nT within 4–5 h. The magnetic field magnitude then sharply increases to around 100 nT at 0 UT 5 February before decreasing to approximately 70 nT within the subsequent hour. After this period, the magnetic field stays within the 60–95 nT range. Between 12 and 18 UT, 4 February, we observe a steady increase in the magnetic field stretching angle from around 60° to 75°. From 18 to 20 UT, the magnetic field stretching angle decreases from 75° to 65° before a quick increase back up to 80°. At around 21 UT, the magnetic field stretching angle decreases abruptly from 80° to around 35° within a 30 min period. From this point, the stretching angle is highly dynamic although trends downward reaching a minimum of about 15° between 1 and 2 UT 5 February. It is noted that the spacecraft is situated in the dusk sector during this highly variable period.

5.5. Phase Space Density

[30] Calculated phase space density as a function of time and L^* with fixed values of μ and K (μ = 500 MeV/G and $K = 2500\ \mathrm{G}^{1/2}\mathrm{km}$ ($\sim 0.4\ \mathrm{G}^{1/2}R_E$)) is shown in Figure 4f. Initially, (from 12 to 18 UT 4 February) a decrease in phase space density is observed with L^* varying between 5.8 and 6.6. From 17 to 22 UT, we see a sizeable decrease in the L^* parameter, indicating that GOES-13 is now on a drift shell that was previously closer to the Earth. From 22 UT 4 February to around 0 UT 5 February, a large increase in the PSD is observed while L^* only increases slightly, between 4.6 and 5.4. The PSD then remains high and L^* between 4.7 and 5.5 for the remainder of the period of interest (until 6 UT 5 February).

5.6. Discussion

[31] From 12 to 17 UT 4 February, we observe a slow, steady increase in electron flux yet the calculated phase space density decreases greatly. This is attributed to a change in the pitch angle distribution of the electrons, and thus, we observe a decrease in phase space density at our chosen K. The flux values support this explanation (see Figures 4e and 6c). As the flux increases steadily, the orientation of the electrons becomes more perpendicular to the magnetic field and therefore at our chosen K value, equivalent to around 30° at this time, we observe a decrease in electron flux and thus phase space density. L^* during this period (12–15 UT) displays an increase from 6.0 to 6.5 and then a decrease back to 6.0 between 15 and 17 UT. While from 12 to 15 UT, discrepancies between the measured magnetic field by GOES-13 and the output of T96 are relatively small (a maximum of around 10 nT in magnitude and 10° in stretching angle), from 15 to 17 UT, these discrepancies increase (a maximum of around 35 nT in magnitude and almost 20° in stretching angle), indicating that the errors highlighted in Figure 1 must be considered and that interpretation PSD results during this period should be approached with caution.

[32] Between 17 and 21 UT, the 475 keV electron flux reduces by around 3 orders of magnitude with a sharp boundary from a peaked pitch angle distribution to an isotropic or even butterfly distribution occurring at 19 UT (see Figure 6c). During this period, we observe a large decrease in the L^* parameter (outward radial transport of electrons). However, the magnetic field magnitude measured by GOES-13 shows discrepancies to that produced by the T96 model. Between 15 and 19 UT, output from T96 predicts a weaker magnetic field than that observed by GOES-13, whereas from around 20 UT 4 February to the end of the period of interest at 6 UT 5 February, the output from T96 predicts a stronger magnetic field than that measured by GOES-13. Between 21 and 0 UT, the error in magnetic field magnitude is largest, implying that the calculated L^* during this period may well be an overestimate since $|B_{T96}| >> |B_{GOES}|$. In this event, the stretching angle from T96 follows the measured stretching angle relatively closely, and therefore, the magnitude errors are likely to be more significant in affecting the calculated PSD and L^* (as described in Figure 1). Again, it appears that transport, adiabatic or otherwise, contributes substantially to this dropout event. The pitch angle distribution displays similar structure to that observed for Event 1 (Figures 6b and 6c); a highly peaked distribution immediately prior to the dropout, with a sharp boundary between a peaked distribution and an isotropic/butterfly distribution apparent, while the omnidirectional electron fluxes are still decreasing. This sharp transition occurs as the solar wind

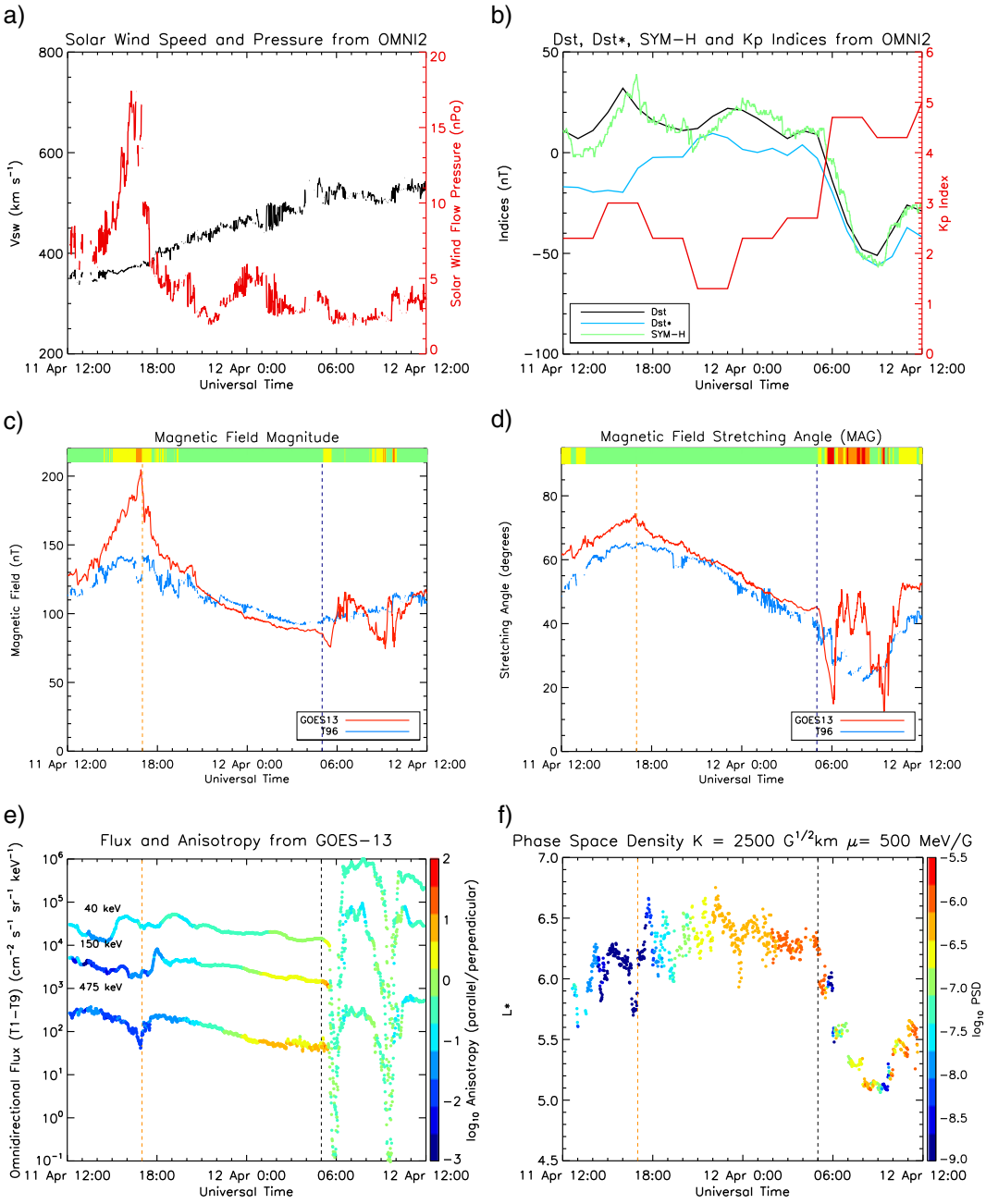

Figure 5. Event 3: 12 UT 11 April to 12 UT 12 April. This figure displays the same parameters as described in Figure 2.

pressure decreases. It is noted however that this similarity in evolutionary structure could at least partly be due to the similar position of GOES-13 in local time during these dropout events.

6. Event 3: 11 April 2011

[33] Figure 5 displays the same parameters as described in Figure 2 for the period of interest highlighted for Event 3 in Table 1.

6.1. Solar Wind and Geomagnetic Conditions

[34] The solar wind speed for this event (see Figure 5a) exhibits a slow increase from around 350 km s^{-1}, at 12 UT 11 April, up to around 550 km s^{-1} by 5 UT 12 April. The pressure is observed to increase, as is characteristic of a high-speed solar wind stream, peaking around 17 UT 11 April. The *Kp* index displays a small increase coincident with the enhanced solar wind pressure before a subsequent decrease. It is not until later (around 5 UT 12 April) that we see a larger increase in *Kp* (coincident with IMF turning abruptly southward), indicating enhanced magnetospheric convection. Geomagnetic indices *Dst* and SYM-H become increasingly positive between 13 and 17 UT in response to the increased solar wind flow pressure (see Figure 5b). It is not until around 5 UT that the characteristic decrease associated with the main phase is observed.

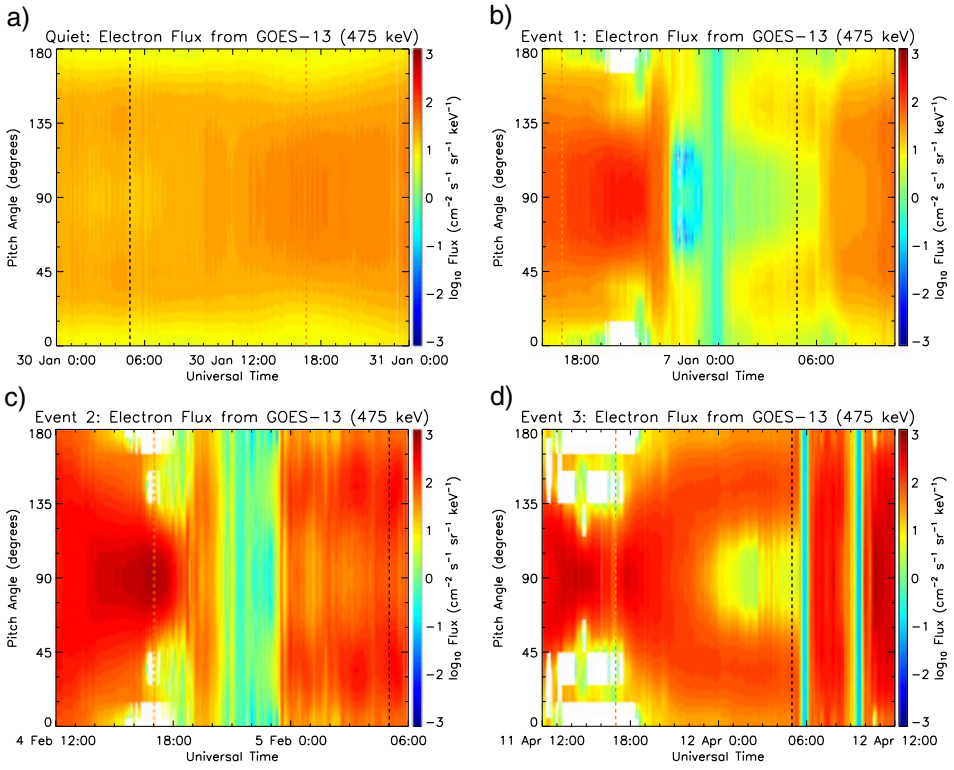

Figure 6. Pitch angle distributions for the quiet event and the three HSS events. Unfilled white areas indicate either bad/missing data or where the fit of the pitch angle distribution to the data produces unrealistically low flux values. These pitch angle distributions are used to calculate the pitch angle anisotropy indicated in Figures 2e, 3e, 4e, and 5e.

6.2. Electron Flux

[35] Electron flux and pitch angle anisotropy are shown in Figure 5e, with the full pitch angle distribution shown in Figure 6d. From 11 April, 12–14 UT, the 475 keV electron flux displays a small increase before decreasing steadily between 14 and 17 UT (around noon local time). This reduction is not observed in the lower energy electron channels. Subsequently, the 475 keV electron flux increases, reaching prereduction values within 1 h (17–18 UT). Throughout this period, the electrons are highly perpendicularly oriented to the magnetic field. From 18 UT 11 April to 5 UT 12 April, the electron fluxes at all measured energies decrease steadily, by almost an order of magnitude. During this reduction, the pitch angle anisotropy of the 475 keV electrons shifts from being highly perpendicularly oriented at 18 UT 11 April, to being highly parallel oriented by 5 UT 12 April. Between 5 and 6 UT 12 April, the electron fluxes rapidly decrease by 3 orders of magnitude. The fluxes then recover rapidly to an elevated level between 6 and 7 UT. Flux measurements undergo a second rapid loss and recovery between 8 and 11 UT. This reduction is similar in magnitude to the first with fluxes reducing by approximately 3 orders of magnitude. During the first of these rapid losses and subsequent recoveries, the pitch angle anisotropy of the 475 keV electrons changes from being highly parallel oriented prior to the reduction to approximately isotropic afterward. During the loss and recovery occurring between 8 and 11 UT, the electron orientation to the magnetic field remains approximately isotropic.

6.3. Pitch Angle Distribution

[36] The pitch angle distribution (see Figure 6d) is initially highly peaked (GOES-13 on the dayside, 12–18 UT 11 April). Between 18 UT 11 April and 5 UT 12 April, the distribution steadily turns butterfly with increasing fluxes more parallel oriented to the magnetic field and decreasing fluxes perpendicularly oriented to the magnetic field. Between 5–6 UT and 9–10 UT 12 April, the flux across the entire distribution falls to very low values. Almost immediately after, the flux promptly becomes elevated at all pitch angles (isotropic). The pitch angle distribution follows the following sequence during this dropout event: (i) highly peaked distribution, (ii) steady turning to butterfly distribution as GOES-13 progresses to the nightside, and (iii) two rapid reductions across all pitch angles with prompt isotropic recovery to elevated levels.

6.4. Magnetic Field

[37] Magnetic field magnitude and stretching angle as measured by GOES-13 are displayed in Figures 5c and 5d. Between 13 and 17 UT 11 April, the measured magnetic field strength exhibits a clear increase from approximately 120 to 200 nT. The peak magnetic field strength is observed when the spacecraft is located around noon local time. Following this, the magnetic field strength decreases steadily for approximately 12 h (17 UT 11 April to 5 UT 12 April) from around 200 to 85 nT, with the minimum coincident with when the spacecraft is located at midnight local time. At 5 UT 12 April, the magnetic field magnitude reduces slightly,

by around 10 nT, before increasing to over 110 nT. A second reduction in magnetic field strength (to around 85 nT) is observed between 7 and 9 UT. Between 9 and 10 UT, GOES-13 measures a spike in the magnetic field magnitude of about 30 nT. Between 10 and 12 UT 12 April, the magnetic field strength increases steadily, reaching around 115 nT by 12 UT. The magnetic field stretching angle from 13 to 17 UT 11 April displays a steady increase from approximately 60° to 75°. The peak in stretching angle (most dipolar) is coincident with when the spacecraft is positioned at noon local time. From 17 UT 11 April to 5 UT 12 April, the magnetic field stretching angle decreases steadily from around 75° to 45°. Just after midnight local time (5 UT 12 April), GOES-13 measures a large change in the stretching of the magnetic field from 45° to around 15° within a period of little over 1 h. The stretching angle then rapidly increases again from 15° to 50° in the following hour (6–7 UT). The stretching angle then exhibits a second large decrease and rapid increase between 2 and 5 UT 12 April with similar magnitude to the first.

6.5. Phase Space Density

[38] Calculated phase space density as a function of time and L^* with fixed values of μ and K (μ = 500 MeV/G and K = 2500 $G^{1/2}$km ($\sim$ 0.4 $G^{1/2}R_E$)) is shown in Figure 5f. The phase space density during 12–16 UT 11 April shows a small decrease while L^* increases slightly from around 5.7 to 6.3. Following this, we observe a sudden decrease and subsequent increase in L^* while the PSD remains low (16–18 UT). This occurs approximately coincident to the small reduction in the measured 475 keV electron flux. From 18 UT 11 April to 5 UT 12 April, the phase space density increases by several orders of magnitude while the L^* parameter remains within the 5.9 to 6.8 range. From 5 to 9 UT 12 April, L^* decreases from around 6.3 to 5.1 with the minimum L^* occurring at the same time as the second rapid reduction and subsequent increase in the measured 475 keV electron flux (8–10 UT 12 April). During this reduction in L^*, the PSD is highly dynamic, reducing rapidly when the electron flux decreases and increasing when the electron fluxes are elevating. These variations of around 3 orders of magnitude in the PSD occur on timescales of 1–2 h. From 10–12 UT 12 April, the PSD values are high with L^* values increasing from around 5.1 to 5.7.

6.6. Discussion

[39] We consider this event in three stages: 12 UT 11 April to 18 UT 11 April, 18 UT 11 April to 5 UT 12 April, and 5 UT 12 April to 12 UT 12 April.

[40] First, the small reduction in 475 keV electron flux observed centered around noon local time (16–18 UT) occurs simultaneous to a large increase in the magnetic field magnitude measured by GOES-13. This appears to be compression of the magnetosphere, increasing the magnetic field strength and transporting electrons inward from GEO. However, the L^* values calculated using the T96 magnetic field model do not support this explanation. At the time of the reduction of 475 keV electron flux, the magnetic field model suggests an L^* decrease, corresponding to outward transport of electrons. Clearly, there is some disagreement between the measurements from GOES-13 and the calculated L^* parameter. A likely cause of this discrepancy would be a large disagreement between the T96 output and the actual geomagnetic field, causing phase space density and L^* values to not be truly representative (larger discrepancy in magnitude colored orange at 17 UT). While from 12 to 15 UT 11 April, we observe that the T96 model and the measured magnetic field from GOES-13 are in relative agreement; from around 15 to 19 UT, the measured magnetic field magnitude is much larger than that predicted by T96 with the greatest difference of around 80 nT occurring just before noon local time (16–17 UT). At the time of this large difference, a small reduction in the T96 magnetic field strength can be seen (about 15 nT), when in reality, the local geomagnetic field strength is increasing (see Figure 5c). This is coincident with the time that we see the rapid decrease and subsequent increase in the L^* parameter. It is therefore a fair assumption to say that the inaccuracies in the T96 magnetic field model at this time/position are causing this discrepancy, and thus, the phase space density and L^* at this time are unlikely to be a true representation of reality. The primary reason for the discrepancy is likely to be the input pressure limit of the T96 magnetic field model (10 nPa), given that the solar wind pressure is quite high during this time.

[41] Second, the electron flux measurements from 18 UT 11 April to 5 UT 12 April display a steady reduction while becoming increasingly parallel oriented with respect to the magnetic field. During this time, the phase space density increases by about 3 orders of magnitude. This is due to our selection of constant K and the changing pitch angle distribution to be more parallel in orientation as the spacecraft moves to the nightside.

[42] Third, between 5 and 12 UT 12 April, we observe two rapid variations in the electron flux at all observed energies. Reductions in electron flux occur at times when the magnetic field, as measured by GOES-13, is highly stretched with the subsequent increases in electron flux occurring as the magnetic field quickly returns to a less stretched state (dipolarizations). This appears to be due to substorm activity injecting high levels of isotropic plasma (as shown in the pitch angle distribution in Figure 6d). The phase space density during this period displays rapid decreases when the flux decreases. Calculated L^* values begin to reduce at the time of the first decrease in electron flux and continue to reduce until the second reduction of electron flux. The shape of this L^* variation appears to match the stretching angle output from the T96 magnetic field model. However, the measured stretching angle from GOES-13 displays large discrepancies (up to almost 30°) from the T96 model output during this time (shown in red and orange on the discrepancy indicator in Figure 5d). This leads to the conclusion that the L^* variation shown between 5 and 12 UT 12 April in Figure 5e is not accurate. It would seem more likely for L^* to decrease while the field is becoming stretched and for L^* to increase during the period when electron flux is returning and the field is becoming less stretched (dipolarizing).

[43] The initial loss (around 17 UT, noon LT) can be attributed to the magnetosphere compressing due to an increase in the solar wind flow pressure causing the magnetic field magnitude to increase. The two sudden variations in electron flux between 5 UT and 12 UT are likely caused due to substorm activity given the position in local time, the

signatures in the measured magnetic field, and the elevated electron flux that follows.

7. Summary and Conclusions

[44] None of the events studied here have particularly large *Dst*, *Dst**, or SYM-H signatures, yet a substantial dropout of the electron flux is still apparent [cf. *Borovsky and Denton*, 2009; *Morley et al.*, 2010; *Meredith et al.*, 2011; *Turner et al.*, 2012; *Hendry et al.*, 2012]. In many respects, such events are more straightforward to analyze compared to large storm events driven by coronal mass ejections.

[45] For Event 1, it is clear that outward adiabatic radial transport plays a key role, with loss of electrons to the magnetopause. However, given the reduction in PSD at an L^* of approximately 5, it appears that there is a loss process, differing from adiabatic transport, acting also. This could be outward radial diffusion caused by a steep radial gradient in the PSD following magnetopause losses and/or pitch angle scattering leading to atmospheric losses.

[46] For Event 2, it appears that the reduction in electron flux at GEO is largely attributable to outward radial transport of electrons based upon the decrease in L^*. However, given the discrepancies between the output of the T96 magnetic field model and the magnetic field measured by GOES-13 during this event, it is not apparent how accurate these PSD and L^* values may be. Therefore, caution must be used when interpreting data for this period due to the errors highlighted in Figure 1.

[47] For Event 3, there is not a well-defined dropout period observed (GOES-13 on the dayside). Instead, we observe a compression of the magnetosphere, causing a small reduction in electron flux around local noon (17 UT) before a steady reduction in electron flux and shift in pitch angle anisotropy. This could be due to local time variations as GOES-13 progresses in orbit. The rapid variations in the electron flux at all observed energies at 5 and 12 UT 12 April are concluded to be substorm activity, based upon the position of the satellite in local time, the observed magnetic field variations, and the elevated electron flux that follows.

[48] The progression of GOES-13 through local time complicates interpretation of electron measurements somewhat; however, this is clearly not the only factor causing variability between HSS events.

[49] The electron dropouts associated with Event 1 and Event 2 display similar structure. This is most evident when studying the full pitch angle distributions in Figures 6b and 6c. Immediately prior to both dropouts, the pitch angle-distributions become highly peaked (increasing fluxes perpendicular to the magnetic field, decreasing fluxes parallel to the magnetic field). Additionally, midway through both dropout periods, while the 475 keV electron fluxes are still falling, a clearly defined transition from a peaked distribution to an isotropic, or even butterfly, distribution is evident as the solar wind pressure begins to decrease. The fluxes then fall to very low values at all pitch angles. These distributions compare well with the averaged pitch angle-resolved fluxes from Los Alamos Satellites also at GEO [*Borovsky and Denton*, 2011b].

[50] Based upon our study of the impact of three high-speed stream events on electron fluxes at geosynchronous orbit, we conclude the following:

[51] 1. There is a high degree of variability in electron flux measurements, the magnitude and duration of the dropout, and the calculated phase space density between HSS events that appear similar based upon solar wind observations.

[52] 2. Outward adiabatic transport plays a key role in causing radiation belt flux dropouts at GEO. This can then lead to magnetopause losses and subsequent outward radial diffusion. Other loss processes may also play a role.

[53] 3. While calculating the phase space density is an invaluable tool for interpreting variation in the radiation belts, due to discrepancies between output from magnetic field models and in situ measurements, it is necessary to consider our calculations in the broader context of additional observed parameters (electron fluxes and magnetic field measurements).

[54] 4. The pitch angle distributions for Events 1 and 2 display similar structure: highly peaked distribution immediately prior to the dropout with a sharp boundary between a peaked distribution and an isotropic/butterfly distribution apparent as the solar wind pressure decreases. Following this, the electron flux steadily decreases to a minimum across the entire distribution.

[55] Adiabatic transport of electrons, leading to magnetopause losses (since the last closed drift shell moves to lower L^*) and subsequent outward radial diffusion, plays a significant role in causing electron dropouts at GEO; however, other loss mechanisms are also a factor (wave-particle interactions and loss to the atmosphere). Future work using coincident measurements of in situ wave phenomena from the Van Allen Probes Mission and of particle precipitation into the atmosphere (e.g., BARREL [*Millan and the BARREL Team*, 2011] and *Clilverd et al.* [2012]) is certain to further our understanding of these important mechanisms.

Appendix A: Pitch Angle Distribution Retrievals From GOES 13-15 Magnetospheric Electron Detector (MAGED) Observations

[56] The purpose of the method outlined here is to invert an accurate pitch angle distribution (PAD), with self-consistent error bars, from multiple telescope measurements that have broad fields-of-view. This approach was motivated in part by the authors' experience that sums of powers of trigonometric functions are very frequently inadequate for fitting MAGED PADs. Moreover, an algorithm that treats the measurements as points in pitch angle space is likely to introduce biases in the fitted PADs. This problem was solved for the Polar High Sensitivity Telescope by *Selesnick and Blake* [2000] using optimal estimation [*Rodgers*, 1976; *Tarantola and Valette*, 1982]. In this development, we have followed *Selesnick and Blake* [2000] closely, using the familiar matrix notation of *Rodgers* [1976], with the necessary changes to account for the three-axis stabilized GOES spacecraft and the MAGED instrument characteristics.

[57] The basic problem is the inversion of the measurement integral. The observed quantity is the number of counts R_{ik} measured during the accumulation period for each energy channel i at each look direction (telescope) k, and we wish to estimate the differential flux $j(E, \theta, \phi)$ on a regular pitch

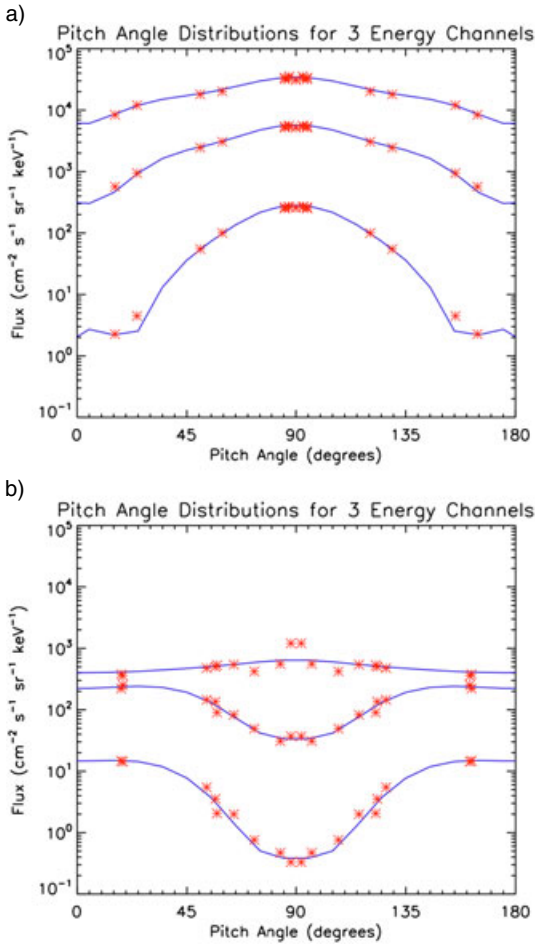

Figure A1. Examples of PADs (peaked and butterfly) obtained using the retrieval code as described in the appendix for energy channels: 40 keV, 150 keV, and 475 keV. The blue line indicates the retrieved PAD with red stars, indicating the measurements from GOES-13.

angle grid. The count rate is related to the differential flux by the measurement integral:

$$R_{ik} = \iint j(E,\theta,\phi)\, A_{ik}(E,\theta,\phi)\mathrm{d}\Omega\, \mathrm{d}E \tag{A1}$$

where $A_{ik}(E,\theta,\phi)$ is the effective area (cm^2) of channel i from telescope k at particle kinetic energy E and direction (θ,ϕ). We identify the polar angle θ with pitch angle α and the azimuth ϕ with the gyroangle β. The cylindrically symmetric and energy-independent modeled MAGED A_{ik} is a good approximation of the measured response [*Hanser*, 2011]. Therefore, we treat A_{ik} as a function only of θ_t (the polar angle from the telescope axis). Its energy independence allows us to treat the energy spectrum estimate separately and therefore to replace the energy integral at this step with the product of the flux at average energy $\overline{E}_i$ and the channel energy bandwidth δE_i [*Hanser*, 2011].

[58] The telescope axis angle is related to the pitch angles and gyroangle as follows:

$$\cos\theta_t = \cos\alpha_o \cos\alpha + \sin\alpha_o \sin\alpha \cos\beta \tag{A2}$$

where α_o is the central pitch angle of a given telescope. Using this transformation and the energy independence of A_{ik}, the integral is rewritten as follows:

$$R_{ik} = \delta E_i \int j(\overline{E}_i,\alpha)\, G_k(\alpha)\mathrm{d}\alpha \tag{A3}$$

$$G_k(\alpha) = \sin\alpha \int_0^{2\pi} A_k[\overline{E}_i \theta_t(\alpha,\beta)]\mathrm{d}\beta \tag{A4}$$

The quantity G_k, the response function of telescope k, has units cm^2 rad and is defined from 0 to 180° pitch angle. It is identically zero at 0 and 180°, due to the $\sin\alpha$ factor, and is positive in between.

[59] Setting vector **y** equal to the set of measured count rates and vector **x** equal to the desired differential fluxes, these integrals are expressed approximately in terms of a matrix multiplication with the weighting function matrix **K** relating **y** and **x**:

$$\mathbf{y} = \mathbf{K}\mathbf{x} \tag{A5}$$

The weighting function **K** is a discrete function given by the product $G_k(\alpha)\ \Delta\alpha\ \delta E_i$ and has units cm^2 sr keV. The value of the weighting function depends on the angular sampling of the telescope response function used in the retrieval and therefore the intervals on which the fluxes are retrieved: The coarser the sampling, the larger the value of the weighting function. The integral for calculating G_k on the equally spaced α output grid is evaluated by calculating A_k for θ_t at each α, stepping β from 0 to 2π. Since the telescope central pitch angles vary with time, G_k must be recalculated at each time step.

[60] The desired differential fluxes **x** and their covariances **S** are estimated as follows [*Rodgers*, 1976]:

$$\mathbf{x} = \mathbf{x_o} + \mathbf{S_x}\,\mathbf{K^T}\left(\mathbf{K}\,\mathbf{S_x}\,\mathbf{K^T} + \mathbf{S_e}\right)^{-1}(\mathbf{y} - \mathbf{K}\,\mathbf{x_o}) \tag{A6}$$

$$\mathbf{S} = \mathbf{S_x} - \mathbf{S_x}\,\mathbf{K^T}\left(\mathbf{K}\,\mathbf{S_x}\,\mathbf{K^T} + \mathbf{S_e}\right)^{-1}\mathbf{K}\,\mathbf{S_x} \tag{A7}$$

$\mathbf{S_e}$ is the covariance matrix of the measurements **y**. Following *Selesnick and Blake* [2000], we define $\mathbf{S_e}$ as a diagonal matrix whose elements (corresponding to each channel) are the sums of the error variances due to counting statistics and other sources of error such as on-orbit lossy compression.

[61] The quantities $\mathbf{x_o}$ and $\mathbf{S_x}$ are the a priori estimate and its covariance matrix, which are required constraints for this underdetermined problem. Much of the challenge lies in selecting appropriate a priori constraints. We set $\mathbf{x_o}$ equal to the omnidirectional average of the measured fluxes, although there is little difference in the results from setting it to zero, as *Selesnick and Blake* [2000] do. Following *Tarantola and Valette* [1982], we define the elements of the a priori covariance matrix as follows:

$$S_x(\alpha,\alpha_o) = \sigma^2 \exp\left[-\frac{1}{2}\frac{(\alpha-\alpha_o)^2}{\Delta^2}\right] \tag{A8}$$

The correlation length Δ is set to the full width at half maximum of the telescope field-of-view [*Selesnick and Blake*, 2000]. The coefficient σ^2 is set equal to the variance in the measurements (at a given energy) about the omnidirectional average $\mathbf{x_o}$. The covariance matrices represent absolute errors, in differential flux units squared. The reported uncertainties on each of the retrieved PAD points are the square roots of the diagonal elements of the covariance matrix **S**.

[62] The pitch angle α is defined only from 0 to 180°. Because of the sparse angular sampling of MAGED, fluxes measured at center pitch angles greater than 90° are assigned to the supplementary angles (180° – α); the 90–180° variation is set to the 90–0° variation to define the full input PAD from 0 to 180°. In order to constrain the solution at the 0 and 180° end points, we extend the input vector **y** cyclically to –90° and +270°. Only flux values for pitch angles between 0 and 180° are reported. In the present work, the output **x** is defined on a 10° grid starting at 5°.

[63] A benefit of optimal estimation is that the output covariance matrix **S** represents the propagation of the measurement errors and a priori assumptions through the inversion, enabling a self-consistent estimate of the retrieval error at each point on the output grid. The advantage of this linear inversion is its relative simplicity, requiring only one matrix inversion (per energy channel) and no iterations. The drawback is that due to the lack of a positivity constraint, one or more negative fluxes are reported occasionally in a PAD, often when one measured point in the PAD is very low. In the current work, such PADs are rejected, leaving a sufficient number of valid PADs for the purpose at hand. A nonlinear, iterative retrieval involving a positivity constraint, which is planned, would be more generally valid but also much slower than the present method.

[64] Figure A1 displays examples of the results from this PAD retrieval method for both peaked and butterfly PADs.

[65] **Acknowledgments.** Research at Lancaster is supported by a Science and Technology Facilities Council (STFC) studentship grant. M.H. Denton is supported by STFC grant ST/I000801/1. OMNI data were obtained from the GSFC/SPDF OMNIWeb interface at http://omniweb.gsfc.nasa.gov. We thank Kyoto University for *Dst* index and SYM-H values and the National Geophysical Data Center for *Kp* index values.

[66] Masaki Fujimoto thanks Steven Morley and an anonymous reviewer for their assistance in evaluating this paper.

References

Borovsky, J. E., and M. H. Denton (2006), Differences between CME-driven storms and CIR-driven storms, *J. Geophys. Res.*, *111*, A07S08, doi:10.1029/2005JA011447.

Borovsky, J. E., and J. T. Steinberg (2006), The calm before the storm in CIR/magnetosphere interactions: Occurrence statistics, solar-wind statistics, and magnetospheric preconditioning, *J. Geophys. Res.*, *111*, A07S10, doi:10.1029/2005JA011397.

Borovsky, J. E., and M. H. Denton (2009), Relativistic-electron dropouts and recovery: A superposed epoch study of the magnetosphere and the solar wind, *J. Geophys. Res.*, *114*, A02201, doi:10.1029/2008JA013128.

Borovsky, J. E., and M. H. Denton (2010), Magnetic field at geosynchronous orbit during high-speed stream-driven storms: Connections to the solar wind, the plasma sheet, and the outer electron radiation belt, *J. Gephys. Res.*, *115*, A08217, doi:10.1029/2009JA015116.

Borovsky, J. E., and M. H. Denton (2011a), Evolution of the magnetotail energetic-electron population during high-speed-stream-driven storms: Evidence for the leakage of the outer electron radiation belt into the Earth's magnetotail, *J. Gephys. Res.*, *116*, A12228, doi:10.1029/2011JA016713.

Borovsky, J. E., and M. H. Denton (2011b), A survey of the anisotropy of the outer electron radiation belt during high-speed-stream-driven storms, *J. Gephys. Res.*, *116*, A05201, doi:10.1029/2010JA016151.

Boscher, D., S. Bourdarie, P. O'Brien, and T. Guild (2008), ONERA-DESP IRBEM library V4.2, 2004-2008, Toulouse France; Aerospace Corporation, Washington, D. C., USA.

Chen, Y., G. D. Reeves, and R. H. Friedel (2007), The energization of relativistic electrons in the outer Van Allen radiation belt, *Nat. Phys.*, *3*, 614–617, doi:10.1038/nphys655.

Clilverd, M. A., C. J. Rodger, D. Danskin, M. E. Usanova, T. Raita, T. Ulich, and E. L. Spanswick (2012), Energetic particle injection, acceleration, and loss during the geomagnetic disturbances which upset Galaxy 15, *J. Geophys. Res.*, *117*, A12213, doi:10.1029/2012JA018175.

Clilverd, M. A., et al. (2013), Energetic electron precipitation characteristics observed from Antarctica during a flux dropout event, *J. Geophys. Res. Space Physics*, *118*, doi:10.1002/2013JA019067, in press.

Denton, M. H., T. Ulich, and E. Turunen (2009), Modification of midlatitude ionospheric parameters in the F2 layer by persistent high-speed solar wind streams, *Space Weather*, *7*, S04006, doi:10.1029/2008SW000443.

Denton, M. H., and J. E. Borovsky (2009), The superdense plasma sheet in the magnetosphere during high-speed-steam-driven storms: Plasma transport time scales, *J. Atmos. Sol. Terr. Phys.*, *71*, 1045–1058, doi:10.1016/j.jastp.2008.04.023.

Denton, M. H., and T. E. Cayton (2011), Density and temperature of energetic electrons in the Earth's magnetotail derived from high-latitude GPS observations during the declining phase of the solar cycle, *Ann. Geophys.*, *29*, 1755–1763.

Elkington, S. R., M. K. Hudson, and A. A. Chan (1999), Acceleration of relativistic electrons via drift-resonant interaction with toroidal-mode Pc-5 ULF oscillations, *Geophys. Res. Lett.*, *26*, 3273–3276, doi:10.1029/1999GL003659.

Freeman, J. W. (1964), The morphology of the electron distribution in the outer radiation zone and near the magnetospheric boundary as observed by Explorer 12, *J. Geophys. Res.*, *69*, 1691–1723.

Friedel, R. H. W., G. D. Reeves, and T. Obara (2002), Relativistic electron dynamics in the inner magnetosphere—A review, *J. Atmos. Sol. Terr. Phys.*, *64*, 265–282, doi:10.1016/S1364-6826(01)00088-8.

GOES N Databook (2009), Prepared for National Aeronautics and Space Administration Goddard Space Flight Center Greenbelt, Maryland 20771 Pursuant to Contract NAS5-98069, Revision C, CDRL PM-1-1-03.

Green, J. C., T. G. Onsager, T. P. O'Brien, and D. N. Baker (2004), Testing loss mechanisms capable of rapidly depleting relativistic electron flux in the Earth's outer radiation belt, *J. Geophys. Res.*, *109*, A12211, doi:10.1029/2004JA010579.

Green, J. C., and M. G. Kivelson (2004), Relativistic electrons in the outer radiation belt: Differentiating between acceleration mechanisms, *J. Geophys. Res.*, *109*, A03213, doi:10.1029/2003JA010153.

Hanser, F. A., (2011), EPS/HEPAD calibration and data handbook, *Tech. rep. GOESN-ENG-048D*, Assurance Technol. Corp., Carlisle, Mass.

Hendry, A. T., C. J. Rodger, M. A. Clilverd, N. R. Thomson, S. K. Morley, and T. Raita (2012), Rapid radiation belt losses occurring during high-speed solar wind stream-driven storms: Importance of energetic electron precipitation, in *Dynamics of the Earth's Radiation Belts and Inner Magnetosphere,* Geophys. Monogr. Ser., vol. 199, edited by D. Summers et al., pp. 213–223, AGU, Washington, D. C., doi:10.1029/2012GM001299.

Huang, C.-L., H. E. Spence, H. J. Singer, and N. A. Tsyganenko (2008), A quantitative assessment of empirical magnetic field models at geosynchronous orbit during magnetic storms, *J. Geophys. Res.*, *113*, A04208, doi:10.1029/2007JA012623.

Hudson, M. K., B. T. Kress, H.-R. Müller, J. A. Zastrow, and J. B. Blake (2008), Relationship of the Van Allen radiation belts to solar wind drivers, *J. Atmos. Sol.-Terr. Phy.*, *70*, 708–729, doi:10.1016/j.jastp.2007.11.003.

Jordanova, V. K., D. T. Welling, S. G. Zaharia, L. Chen, and R. M. Thorne (2012), Modeling ring current ion and electron dynamics and plasma instabilities during a high-speed stream driven storm, *J. Geophys. Res.*, *117*, A00L08, doi:10.1029/2011JA017433.

King, J. H., and N. E. Papitashvili (2005), Solar wind spatial scales in and comparisons of hourly Wind and ACE plasma and magnetic field data, *J. Geophys. Res.*, *110*, A02104, doi:10.1029/2004JA010649.

MacDonald, E. A., L. W. Blum, S. P. Gary, M. F. Thomsen, and M. H. Denton (2010), High-speed stream driven interferences of global wave distributions at geosynchronous orbit: Relevance to radiation-belt dynamics, *Proc. R. Soc. A*, *466*, 3351–3362, doi:10.1098/rspa.2010.0076.

Mann, I. R., T. P. OBrien, and D. K. Milling (2004), Correlations between ULF wave power, solar wind speed, and relativistic electron flux in the magnetosphere: Solar cycle dependence, *J. Atmos. Sol. Terr. Phys.*, *66*, 187–198, doi:10.1016/j.jastp.2003.10.002.

McPherron, R. L., and J. Weygand (2006), The solar wind and geomagnetic activity as a function of time relative to corotating interaction regions, in *Recurrent Geomagnetic Storms: Corotating Solar Wind Streams*, edited by B. T. Tsurutani et al., pp. 125–138, AGU, Washington, D. C., doi:10.1029/167GM12.

McPherron, R. L., D. N. Baker, and N. U. Crooker (2009), Role of the Russell–McPherron effect in the acceleration of relativistic electrons, *J. Atmos. Sol.-Terr. Phy.*, *71*, 1032–1044.

Meredith, N. P., R. B. Horne, M. M. Lam, M. H. Denton, J. E. Borovsky, and J. C. Green (2011), Energetic electron precipitation during high-speed solar wind stream driven storms, *J. Geophys. Res.*, *116*, A05223, doi:10.1029/2010JA016293.

Millan, R. M., and the BARREL Team (2011), Understanding relativistic electron losses with BARREL, *J. Atmos. Sol.-Terr. Phy.*, *73*(11–12), 1425–1434, doi:10.1016/j.jastp.2011.01.006.

Millan, R. M., et al. (2013), The Balloon Array for RBSP Relativistic Electron Losses (BARREL), *Space Sci. Rev.*, *179*, 503–530, doi:10.1007/s11214-013-9971-z.

Miyoshi, Y., A. Morioka, R. Kataoka, Y. Kasahara, and T. Mukai (2007), Evolution of the outer radiation belt during the November 1993 storms driven by corotating interaction regions, *J. Geophys. Res.*, *112*, A05210, doi:10.1029/2006JA012148.

Miyoshi, Y., and R. Kataoka (2008), Flux enhancement of the outer radiation belt electrons after the arrival of stream interaction regions, *J. Geophys. Res.*, *113*, A03S09, doi:10.1029/2007JA012506.

Morley, S. K., R. H. W. Friedel, E. L. Spanswick, G. D. Reeves, J. T. Steinberg, J. Koller, T. Cayton, and E. Noveroske (2010), Dropouts of the outer electron radiation belt in response to solar wind stream interfaces: Global positioning system observations, *Proc. R. Soc. A*, *466*, 3329–3350, doi:10.1098/rspa.2010.0078.

Nagai, T. (1988), Space weather forecast: Prediction of relativistic electron intensity at synchronous orbit, *Geophys. Res. Lett.*, *15*, 425–428.

Onsager, T. G., et al. (2002), Radiation belt electron flux dropouts: Local time, radial, and particle-energy dependence, *J. Geophys. Res.*, *107*(A11), 1382, doi:10.1029/2001JA000187.

Reeves, G. D., K. L. McAdams, R. H. W. Friedel, and T. P. OBrien (2003), Acceleration and loss of relativistic electrons during geomagnetic storms, *Geophys. Res. Lett.*, *30*(10), 1529, doi:10.1029/2002GL016513.

Rodgers, C. D. (1976), Retrieval of atmospheric temperature and composition from remote measurements of thermal radiation, *Rev. Geophys.*, *14*, 609–624.

Selesnick, R. S., and J. B. Blake (2000), On the source location of radiation belt relativistic electrons, *J. Geophys. Res.*, *105*(A2), 2607–2624, doi:10.1029/1999JA900445.

Sojka, J. J., R. L. McPherron, A. P. van Eyken, M. J. Nicholls, C. J. Heinselman, and J. D. Kelley (2009), Observations of ionospheric heating during the passage of solar coronal hole fast streams, *Geophys. Res. Lett.*, *36*, L19105, doi:10.1029/2009GL039064.

Shprits, Y. Y., S. R. Elkington, N. P. Meredith, and D. A. Subbotin (2008a), Review of modeling of losses and sources of relativistic electrons in the outer radiation belt I: Radial transport, *J. Atmos. Sol. Terr. Phys.*, *70*, 1679–1693, doi:10.1016/j.jastp.2008.06.008.

Shprits, Y. Y., D. A. Subbotin, N. P. Meredith, and S. R. Elkington (2008b), Review of modeling of losses and sources of relativistic electrons in the outer radiation belt II: Local acceleration and losses, *J. Atmos. Sol. Terr. Phys.*, *70*, 1694–1713.

Tarantola, A., and B. Valette (1982), Generalized nonlinear inverse problems solved using the least squares criterion, *Rev. Geophys.*, *20*, 219–232.

Thorne, R. M. (2010), Radiation belt dynamics: The importance of wave-particle interactions, *Geophys. Res. Lett.*, *37*, L22107, doi:10.1029/2010GL044990.

Tsurutani, B. T., et al. (2006), Corotating solar wind streams and recurrent geomagnetic activity: A review, *J. Geophys. Res.*, *111*, A07S01, doi:10.1029/2005JA011273.

Tsyganenko, N. A., and D. P. Stern (1996), Modeling the global magnetic field of the large-scale Birkeland current systems, *J. Geophys. Res.*, *101*, 27,187–27,198, doi:10.1029/96JA02735.

Turner, D. L., Y. Shprits, M. Hartinger, and V. Angelopoulos (2012), Explaining sudden losses of outer radiation belt electrons during geomagnetic storms, *Nat. Phys.*, *8*, 208–212, doi:10.1038/nphys2185.

Ukhorskiy, A. Y., M. I. Sitnov, R. M. Millan, and B. T. Kress (2011), The role of drift orbit bifurcations in energization and loss of electrons in the outer radiation belt, *J. Geophys. Res.*, *116*, A09208, doi:10.1029/2011JA016623.